nature nanotechnology

SUPPLEMENTARY INFORMATION

https://doi.org/10.1038/s41565-019-0467-1

In the format provided by the authors and unedited.

Defect induced, layer-modulated magnetism in ultrathin metallic $PtSe_2$

Ahmet Avsar[1,2]*, Alberto Ciarrocchi[1,2], Michele Pizzochero[3], Dmitrii Unuchek[1,2], Oleg V. Yazyev[3] and Andras Kis[1,2]*

[1]Electrical Engineering Institute, École Polytechnique Fédérale de Lausanne (EPFL), Lausanne, Switzerland. [2]Institute of Materials Science and Engineering, École Polytechnique Fédérale de Lausanne (EPFL), Lausanne, Switzerland. [3]Institute of Physics, École Polytechnique Fédérale de Lausanne (EPFL), Lausanne, Switzerland. *e-mail: ahmet.avsar@epfl.ch; andras.kis@epfl.ch

Defect induced, layer-modulated magnetism in ultrathin metallic $PtSe_2$

Ahmet Avsar, Alberto Ciarrocchi, Michele Pizzochero, Dmitrii Unuchek, Oleg V. Yazyev, Andras Kis

1. Temperature dependence of the ultra-thin $PtSe_2$'s resistance

The bottom panel of Supplementary Fig. 1 shows the temperature dependence of the device resistance obtained from a ~ 9 nm thick $PtSe_2$ (device B). The overall device resistance increases as the temperature is increased which provides an additional proof that our $PtSe_2$ crystal is metallic at this thickness range.[1] Similarly to the temperature dependence of the device resistance obtained from a 5.2 nm thick $PtSe_2$ (device A), we observe an anomaly in this sample which could be related to spin dependent scattering.

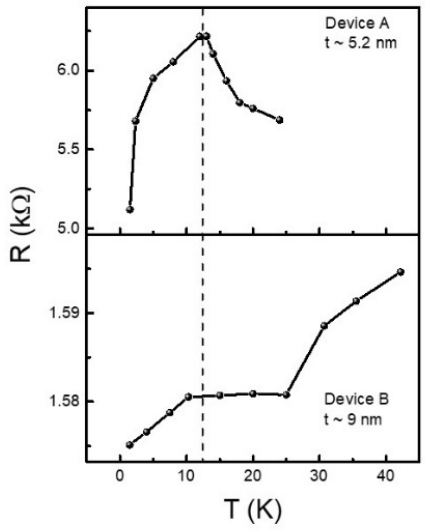

Supplementary Fig. 1. Temperature dependence of the device resistance. The total device resistance as a function of temperature obtained from ~ 5.2 nm (device A, shown in Figure 2) and ~ 9 nm thick $PtSe_2$ crystals. The black dotted line represents the position of the anomaly.

2. Charge transport characterization of device F (~ 2.2 nm thick $PtSe_2$)

Supplementary Fig. 2 shows the charge transport characteristics of a ~ 2.2 nm thick $PtSe_2$ crystal (device F). In sharp contrast to the metallic response observed from relatively thicker samples as shown in Figure 1b and Figure S6, here we observe semiconducting behavior. The device shows p-type behavior with a hole mobility of ~ 32 cm^2/Vs and an on/off ratio of ~ 5×10^4. Observation of non-linear I_{SD}-V_{SD} relation suggests the presence of a Schottky barrier at the contacts. The obtained response is in a good agreement with recent findings.[1,2] We would like to note that it is difficult to probe magnetism in semiconducting flakes under lateral device measurement geometry since signal-to-noise ratio is unfortunately low. In this semiconducting device, we also performed magnetic field dependent measurements. However, here we could not probe the magnetization since noise in the device is much higher than the contribution we would expect from magnetism.

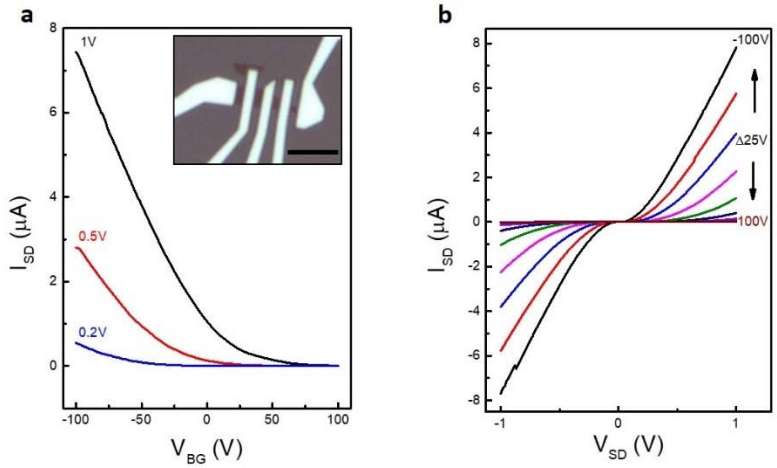

Supplementary Fig. 2. Electrical transport characterization of device F. a, V_{BG} dependence of I_{SD} measured at fixed biases of V_{SD} = 0.2 V, 0.5 V and 1 V. Inset shows the optical image of the characterized device. Black solid line represents the scale bar (5 μm). **b,** V_{SD} dependence of I_{SD} measured at fixed V_{BG} values. Charge transport measurements were performed at 1.5 K.

3. Magnetoresistance measurements in device G (~ 2 nm thick $PtSe_2$)

In our manuscript, we employ a local measurement geometry to probe the magnetism. Since the relative change in device resistance (due to magnetism) is small compared to the total device resistance, we have focused only on metallic samples. It is challenging to measure magneto-transport in crystals thinner than 2.5 nm (as they are very resistive) under such lateral measurement geometry due to low signal-to-noise ratio, as discussed above. Therefore, we prepared a new type of a device to prove that magnetization persists in a few-layer crystals as well. Here, we utilized graphene as a bottom electrode and we transferred ultra-thin $PtSe_2$ on top of graphene. Finally, we formed non-magnetic Pd contacts on graphene and on top of $PtSe_2$. Measurement schematics and optical images of the device are shown in Supplementary Fig. 3**a-c**. The observation of anti-ferromagnetic response in this vertical device demonstrates that even ultra-thin $PtSe_2$ is magnetic.

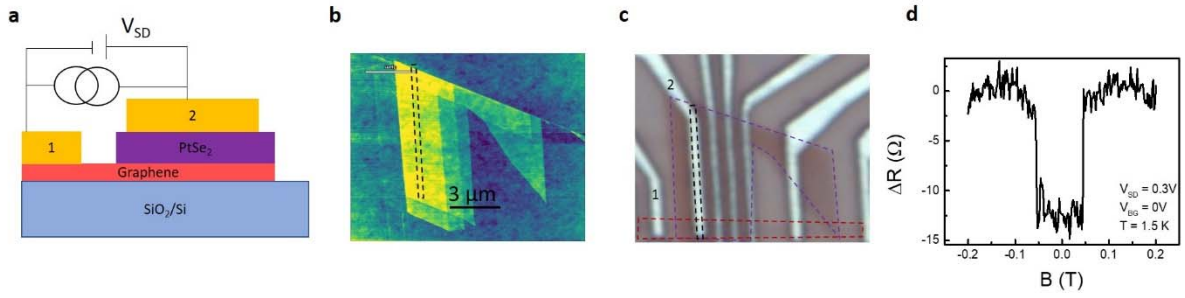

Supplementary Fig. 3. $PtSe_2$-based vertical device. a Measurement configuration. **b** AFM picture of $PtSe_2$ used in device G. **c** Optical picture of a completed device. Red, purple and black dotted lines represent the position of bottom graphene contact, $PtSe_2$ and non-magnetic Pd electrode, respectively. **d** Magneto-transport response obtained in this device. Measurement temperature is 1.5 K.

Due to a complicated device structure (Si/SiO_2/Graphene/$PtSe_2$/top Pd metal contacts), we did not have enough space to place additional contacts in order to study the lateral transport

characteristic of this device. However, we expect this ~ 2 nm thick crystal to be semiconducting. During this study, we measured electrical properties of 13 devices, two of them have thickness of ≤ 2.5 nm. These ultrathin devices exhibit semiconducting behavior. Our results are also in a good agreement with experimental works by A. Ciarrocchi et al.,[1] and X. Yu et al.,[2] that crystals thinner than 2.5 nm show semiconducting behavior. We finally would like to note that our ~ 2 nm thick vertical $PtSe_2$-based device shows antiferromagnetic behavior. It is clear that for insulating systems the RKKY model does not apply, as no Fermi surface can be conceived. For this thickness range, it is difficult for us to estimate the exchange coupling strength. We remark that the investigation of defect-induced magnetism in insulating $PtSe_2$ films does not fall within the scope of the present work, in which we specifically focus on metallic $PtSe_2$ samples.

4. Additional magnetoresistance measurements in device A

Supplementary Fig. 4 shows the dependence of the device resistance on the magnetic field sweep direction. As mentioned in the manuscript, we observe a dip in the resistance around 25 (-25) mT while the field is ramped from -0.2 T (0.2 T) to 0.2 T (-0.2 T) below a critical temperature of 13 K (Supplementary Fig. 4**a**). Next, we repeatedly sweep the field starting from –0.2 T (0.2 T) to 25 mT (-25 mT) where we previously observed the dip, then we sweep the field back to -0.2 T (0.2 T). As shown in Supplementary Fig. 4**b**, the device resistance stays in the same state until the negative (positive) field is applied which polarizes the magnet back to the initial state.

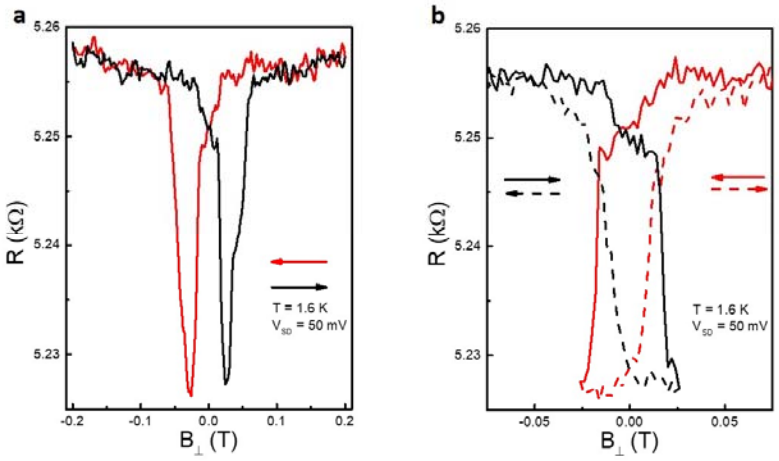

Supplementary Fig. 4. Magnetoresistance measurements in device A. a, Magnetoresistance of $PtSe_2$ as a function of out-of-plane magnetic field. Red (black) arrow represents the sweep direction. **b,** Observation of a minor loop in $PtSe_2$. In this measurement configuration, the device resistance is first measured while the B field is swept from 200 mT to -26 mT (solid red line). Then, the sweep direction is reversed, and the field is swept from -26 mT to 200 mT (dashed red line). The same protocol is applied for the opposite sweep directions as well (Solid and dashed black lines).

5. Additional magnetoresistance measurements in device H

Similarly to the ferromagnetic response observed in Figure 2, we characterized three additional devices which show similar coercive field values, bias and gate dependencies. Supplementary Fig. 5**a** shows the change in device resistance under backward and forward magnetic field sweep directions at fixed bias of V_{SD} = 0.2 V for device H. Differently, this device was studied at the higher bias regime as well (Supplementary Fig. 5**b**). Here, we detect a further reduction in the calculated magneto-resistance percentage as the bias is increased, in good agreement with the tendency observed in Figure 2b.

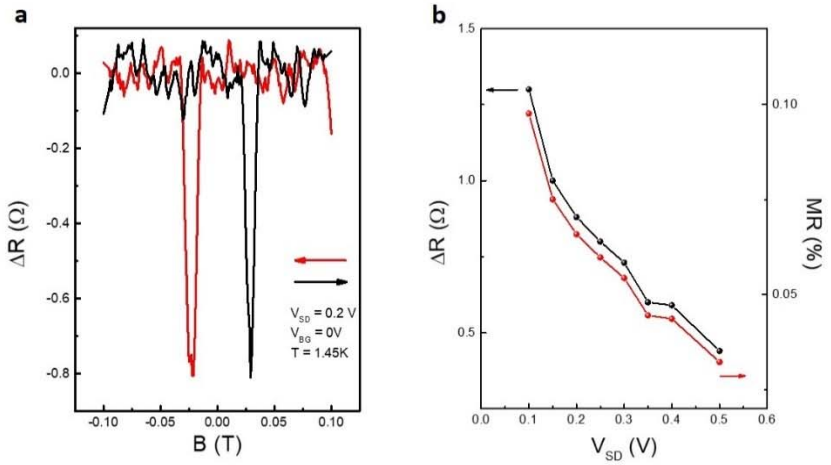

Supplementary Fig. 5. Bias dependent magnetoresistance measurements in device H. a, The change in the device resistance under the forward and backward field sweep directions at fixed V_{SD} = 0.2 V and V_{BG} = 0 V. **b,** V_{SD} dependence of the calculated magneto-resistance percentage. Measurements were taken at V_{BG} = 0 V and T = 1.45 K.

6. Gate voltage dependent measurements in device B

Supplementary Fig. 6**a** shows the gate voltage dependence of the bias current at fixed bias voltage of V_{SD} = 50 mV. Observation of nearly gate-independent response shows the metallic characteristic of this ultra-thin $PtSe_2$. Similarly to the device conductance, the change in the device resistance under magnetic field, ΔR, is also insensitive to V_{BG} as shown in Supplementary Fig. 6**b**. Two-plateau response is observed at V_{BG} = 0, 60, -60 V with identical switching field values.

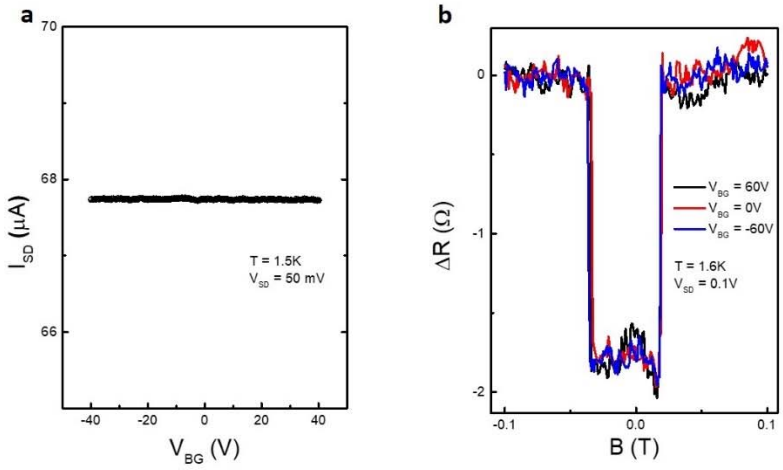

Supplementary Fig. 6. Gate-voltage dependent magnetoresistance measurements in device B. a, V_{BG} dependence of I_{SD} measured at fixed bias of V_{SD} = 50 mV. **b,** Dependence of change in device resistance on the magnetic field at fixed bias of V_{SD} = 0.1 V. Measurements were taken at V_{BG} = 0, 60 and - 60 V and T = 1.6 K.

7. Source-drain bias dependent magnetoresistance measurements in device A

Supplementary Fig. 7**a** shows the dependence of the device resistance on the field at fixed biases of V_{SD} = 5, 7.3, 10, 30 and 50 mV. As the bias is reduced, the magnitude of the change in device resistance increases. The highest value of ~ 400 ohm is observed for the lowest bias of V_{SD} = 1mV (Supplementary Fig. 7**b**). Supplementary Fig. 7**c** shows the dependence of the calculated magnetoresistance change on the applied bias voltage.

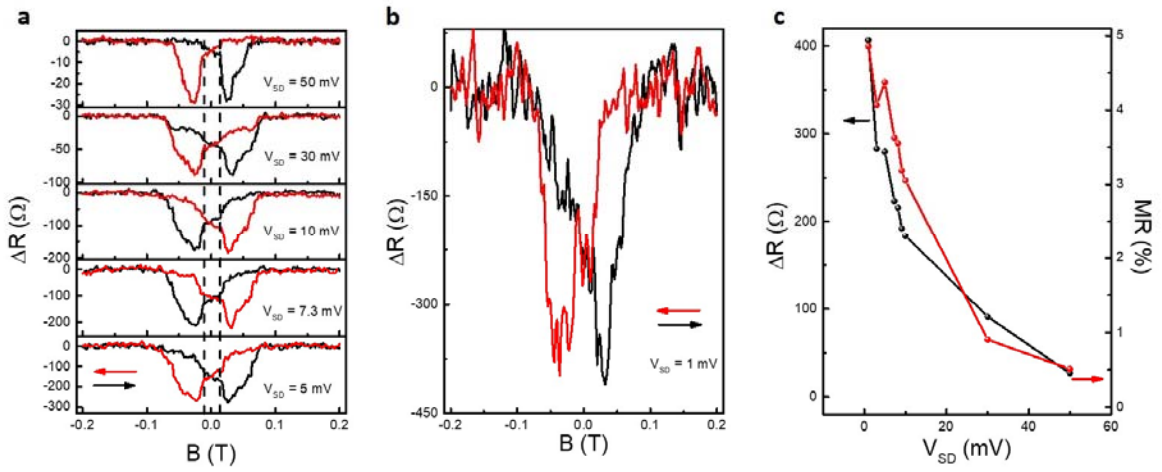

Supplementary Fig. 7. V_{SD} dependent magnetoresistance measurements in device A. a, The change in the device resistance for forward and backward field sweep directions at fixed bias values. Dotted lines represent the appearance of systematic kinks in the magneto-transport measurements which could be related with the switching of different layers at different field values. **b,** Field dependence of the change in device resistance measured at fixed bias value of V_{SD} = 1 mV. **c,** Bias dependence of the calculated magneto-resistance percentage. Measurements were taken at V_{BG} = 0 V and T = 1.5 K.

8. Additional magnetoresistance measurements in device I under large field values

Supplementary Fig. 8 shows the out-of-plane magnetic field dependence of the device current measured at a fixed bias of V_{SD} = 0.1 V. Here, the field is swept from -5 T to 5 T. In addition to the weak antilocalization effect (expected from $PtSe_2$ due to its high spin orbit coupling strength), we observe an anomaly near B = 0 T, similar to Figure 3 (*device B*). As discussed in the manuscript, this anomaly is related with the antiferromagnetic ordering. The signal disappears above a critical temperature (~ 5 K for this device).

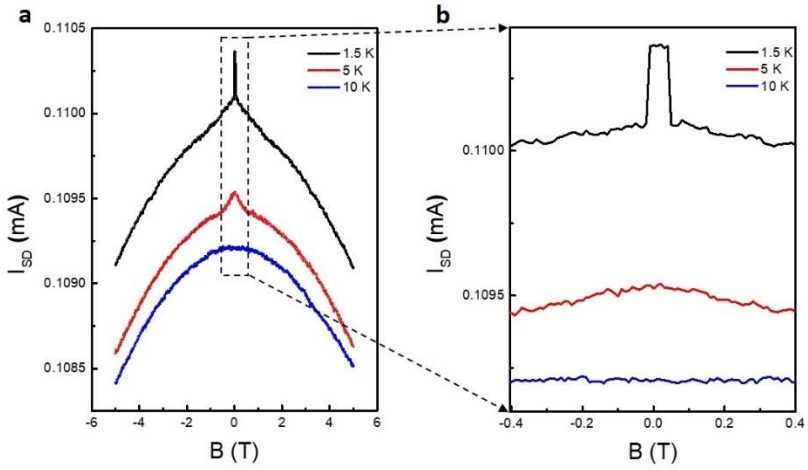

Supplementary Fig. 8. Magnetic field dependence of the bias current. a, Dependence of the bias current on magnetic field at fixed bias of V_{SD} = 0.1 V. The rectangle shape box shows the zoomed-out region of the data shown in **b.** Measurements were taken at T = 1.5, 5 and 10 K.

9. Additional magnetoresistance measurements in device J under large field values

Similarly to the magnetic response shown in Supplementary Fig. 8 and Figure 3 for device I and device B, here we demonstrate two-plateau response obtained from device J (Supplementary Fig. 9). Switching fields are comparable. The signal in this ~ 9 nm thick device disappears above 3.3 K.

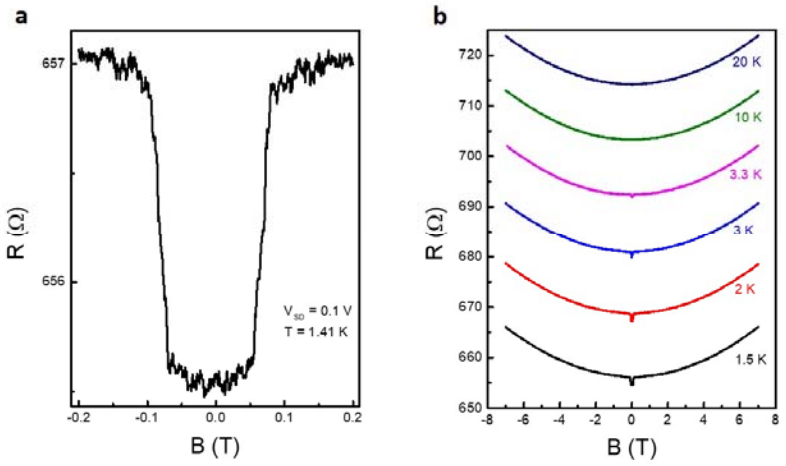

Supplementary Fig. 9. Magnetic field and temperature dependence of the total device resistance. a, Dependence of the device resistance on the magnetic field at fixed bias of V_{SD} = 0.1 V. **b,** Temperature dependence of the signal shown in **a,** but at higher magnetic field range. The field was swept from -7 T to 7 T while the device resistance was being recorded. Measurements were taken at T = 1.5, 2, 3, 3.3, 10, and 20 K.

10. Additional first-principles calculations of vacancy defects

We complete our first-principles investigation of vacancy defects in $PtSe_2$ by considering the Se vacancy defect. Though widely observed in $PtSe_2$, we find that this type of defect does not induce magnetism, as confirmed by inspecting the spin density of the system and as illustrated by the electronic density of states shown in Supplementary Fig. 10**a**. Overall, we find that the presence of Se vacancies has a minor effect on the electronic structure of $PtSe_2$.

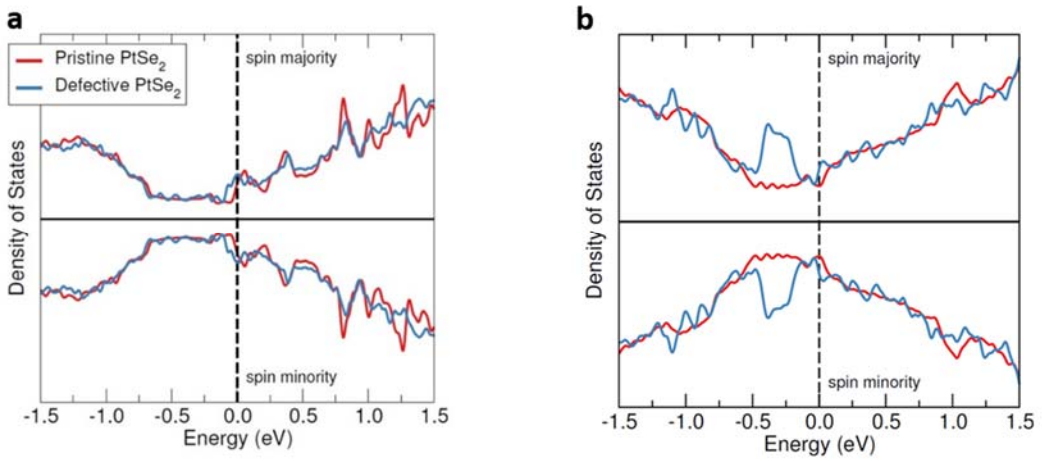

Supplementary Fig. 10. Density of states with and without Se vacancy. Electronic density of states of (a) multilayer $PtSe_2$ with (blue) and without (red) a Se vacancy and (b) bulk $PtSe_2$ with and without a Pt vacancy. Fermi level is set to zero (vertical dashed line).

Next, we consider Pt vacancies in bulk $PtSe_2$. Surprisingly, our calculations show that Pt vacancy defects in bulk $PtSe_2$ are *non-magnetic*, hence there is a pronounced difference between the electronic and magnetic properties of Pt vacancies in bulk and surface locations. This observation points to a *non-uniform* (or *surface*) character of magnetization in thin films of $PtSe_2$. The surface character of magnetism in $PtSe_2$ is supported by the fact no magnetism is experimentally observed in bulk samples of $PtSe_2$, as discussed below (Supplementary Section 12). In the surface magnetism scenario, the interplay between the ferro- and antiferromagnetic configurations of thin films can be explained by the thickness dependent effective magnetic exchange coupling between the surface-localized magnetic moments. As discussed in the main text within the framework of the RKKY model, one can consider $PtSe_2$ thin films as a magnetic bilayer system. Making a rigorous correspondence between the proposed RKKY picture and the results of first-principles calculations goes beyond the scope of this work. Nevertheless, the calculated spin density across the 6-layer slab with Pt vacancy

in layer I clearly supports the RKKY interaction scenario (Supplementary Fig. 11). The large magnetic moment of 1.2 Bohr magneton in layer I induces a decaying spin polarization across the slab that changes its sign upon reaching layer VI, especially clearly visible in the plots of the integrated spin density (panels (c) and (d) of Supplementary Fig. 11).

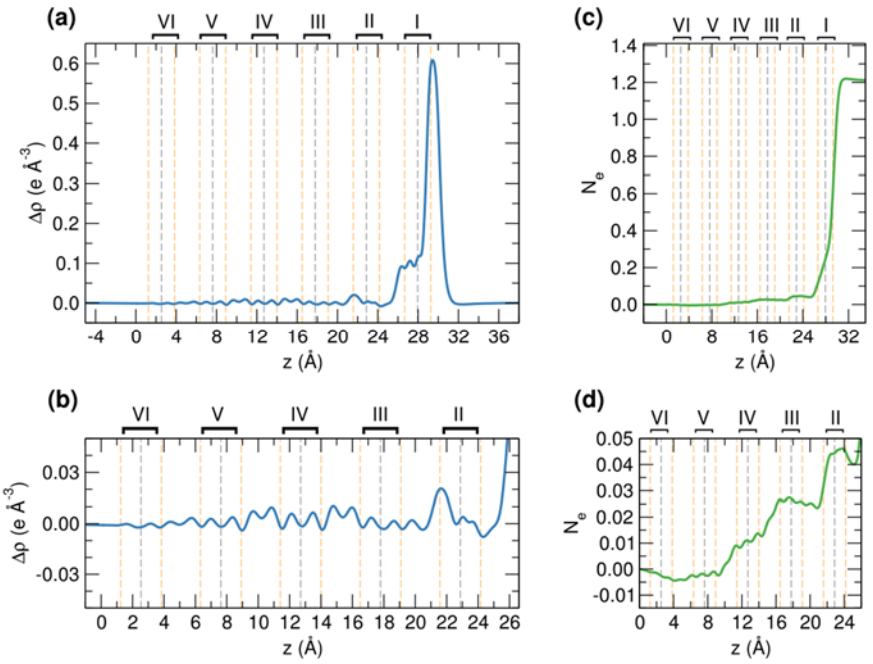

Supplementary Fig. 11. Spin polarization as a function of thickness. a Spin density Δρ(*z*) as a function of out-of-plane position *z* (and averaged in *xy plane*) across the 6-layer slab with a magnetic Pt vacancy defect in layer I. **b** Details of induced spin density Δρ(*z*) in layers II-VI. **c,d** Spin density integrated from 0 to *z* as a function *z*. Panel **d** clearly demonstrates the opposite sign spin polarization in layer VI.

11. Role of exposure to air on electronic and magnetic properties of $PtSe_2$

In order to address the role of air exposure on the electronic and magnetic properties of our samples, we have performed additional experiments and calculations.

As a first step, we evaluate the basic electronic properties of one representative device under controlled conditions. To this end, the device was annealed at 250 °C under high vacuum

conditions to remove potential adsorbates. We note that such high-temperature annealing does not lead to any degradation of the crystal (See Supplementary Fig. 12). This approach was previously adopted to remove contaminants such as O_2 and H_2 from two-dimensional MoS_2[3] and graphene[4], without creating additional defects. After measuring the device resistance under vacuum conditions, we exposed it to air and measured the evolution of its resistance in time. If significant contaminants-induced charge transfer had occured, the device resistance would have shown rapid changes as well as hysteresis in transport measurements.[5] On the other hand, as shown in Supplementary Fig. 12, the transport characteristics of our metallic $PtSe_2$ sample are fully preserved upon air exposure, thereby indicating the electronic properties of the device are not affected.

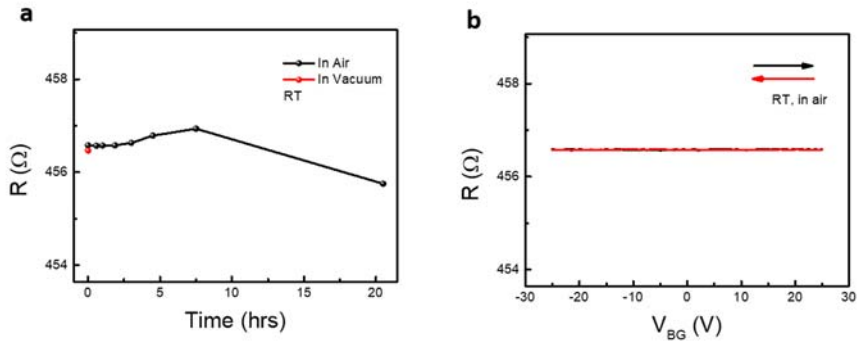

Supplementary Fig. 12. Role of air exposure on electronic properties of $PtSe_2$ (a) Transport characteristics of a ~ metallic $PtSe_2$ device measured under vacuum and air conditions. The device is first measured under vacuum (~ 2×10^{-4} Torr) and then directly exposed to air and measured as a function of time. (b) Back gate voltage dependence of device resistance under backward (red arrow) and forward (black arrow) gate sweeps.

Secondly, we address the magnetic properties of one of our device under controlled conditions. We firstly measure our device at 1.4 K without any annealing treatment. As shown in Supplementary Fig. 13**a**, we observe a ferromagnetic response. Then, we anneal our device at 250 °C under vacuum conditions to desorb possible adsorbates. As shown in Supplementary

Fig. 13**b**, we similarly observe a ferromagnetic response. Note that the shape of switching curves, magnitude of ΔR and coercive fields are almost identical for these two measurements. V_{SD} dependence of ΔR is also almost identical before and after the annealing treatment (Supplementary Fig. 13**c**). These observations suggest that magnetic properties are also preserved after removing the possible adsorbates.

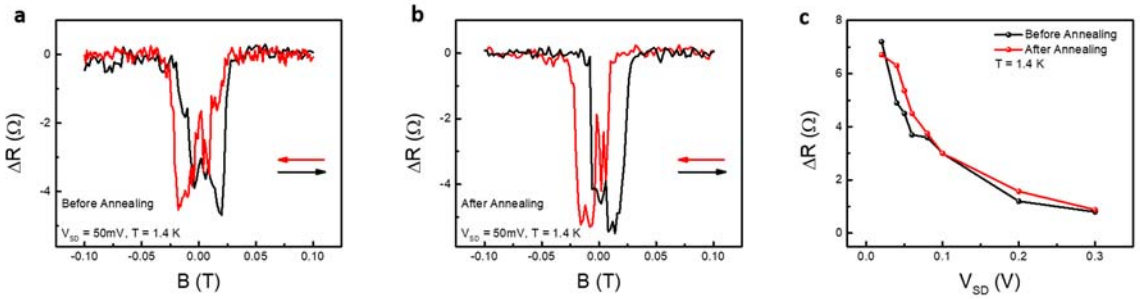

Supplementary Fig. 13. Role of air exposure on magnetic properties of $PtSe_2$. The resistance change under magnetic field acquired at fixed bias of V_{SD} = 50 mV at 1.4 K in an as fabricated device, without any annealing treatment. (b) The resistance change under magnetic field acquired at a fixed bias of V_{SD} = 50 mV at 1.4 K after 250 C annealing. (c) Source-drain bias (V_{SD}) dependences of the change in the device resistance before and after the annealing treatment.

Hence, we conclude from our additional experiments that the electronic and magnetic properties of our samples are preserved upon air exposure. It is worth noticing in this context that recent first-principles calculations[6] found that the dissociation of contaminants (e.g. H_2O) on $PtSe_2$ requires an energy barrier larger than 1.5 eV. This indicates that chemisorption is very unlikely to occur even at relatively high temperatures.

12. Thickness dependent magnetoresistance in $PtSe_2$

Bulk $PtSe_2$ do not show any sign of magnetism. Supplementary Fig. 14 shows the magneto-transport measurements from a bulk sample, where the magnetism-related signals shown in

manuscript are missing. Similarly, magneto-transport studies on thick $PtSe_2$ crystals (60 and 150 nm thick bulk crystals) measured by other groups also do not show any sign of magnetism.[7] They observe a similar B field dependence to our data, as shown in Supplementary Fig. 14. This further suggests that the magnetism we describe in our manuscript occurs only in ultra-thin samples where defects play a critical contribution.

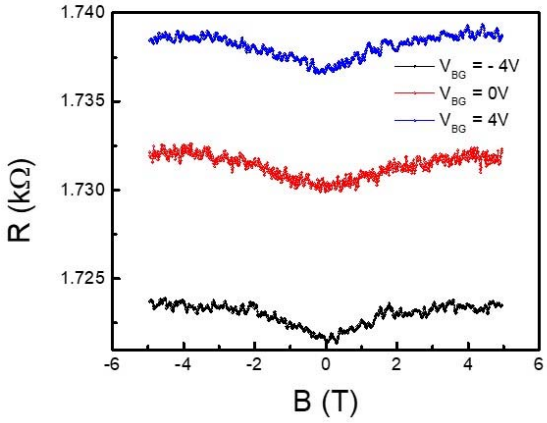

Supplementary Fig. 14. Magneto-transport in ~ 20 nm thick $PtSe_2$. Magnetic field dependence of resistance in bulk $PtSe_2$. Measurement temperature is 1.5 K.

Our thickness dependent measurements, in good agreement with the surface magnetism scenario suggested by our DFT calculations, show that as the thickness of the crystal is increased, the MR decreases. Supplementary Fig. 15 summarizes devices with their thickness, MR magnitude and magnetic behavior. Please see the details of the protocol we followed below.

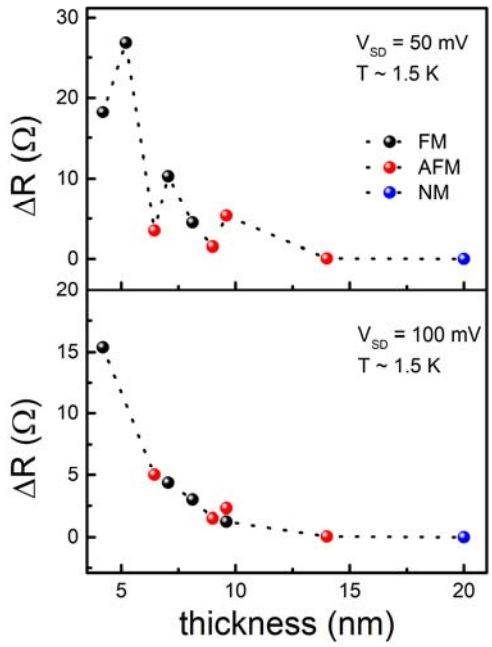

Supplementary Fig. 15. Thickness dependent MR. Thickness dependence of MR curves for studied samples at fixed V_{SD} of 50 mV and 100 mV. Black (red) dots represent devices showing characteristic FM (AFM) response. The blue dot indicates the absence of magnetism in thicker crystals. Error bars in crystal thicknesses have not been included due to the fact that AFM measurements have been performed under different scanning conditions.

As shown in Fig. 2b & Fig. 3b and discussed in manuscript, the measured MR strongly depends on the applied bias. Therefore, we focused on plotting the thickness dependence of MR at fixed biases (V_{SD} = 50 mV and 100 mV). Since we had this insight on strong bias dependence of MR signal after several devices have already been characterized, the first batch of characterized samples was not studied in detail as a function of bias. Therefore, not all measured devices are included in this plot, but only those measured at 50 mV and 100 mV biases. Nevertheless, this summary has three main messages: 1-) MR magnitude decreases as crystal thickness increases, 2-) there is the presence of layer dependent magnetism and 3-) magnetism disappears at thicker crystals.

13. Air Stability of $PtSe_2$

Air-stability of $PtSe_2$ was previously investigated by Y. Zhao et al. through surface and Raman characterization techniques.[6] Here, we perform complementary experiments to demonstrate the air-stability of $PtSe_2$ after a variety of treatments. Our AFM scans demonstrate that ultra-thin $PtSe_2$ (~3.9 nm) does not show any signs of degradation even 3 months after its exfoliation. To further demonstrate its stability, we annealed our crystal at 250 °C. The sample remains pristine even after such annealing step, as shown in Supplementary Fig. 16. We note that well-known crystals such as CrI_3[8] and black phosphorus[9,10] do not exhibit such long-term stability. In this regards, we suggest that metallic $PtSe_2$ stands out from many atomically-thin crystals.

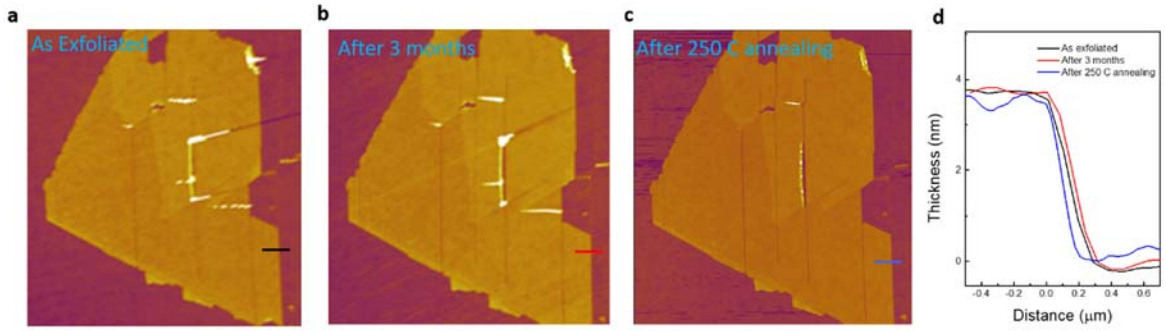

Supplementary Fig. 16. Environmental sensitivity of $PtSe_2$. (a) AFM image taken approximately 1 hour after exfoliation. (b) AFM image of the same flake 3 months after its exfoliation. The flake was stored in the glove-box but no special care was taken: the flake was exposed to air while transferring it between different equipment. (c) The same flake after 250 °C annealing for 1 hour under vacuum conditions (~ 1×10^{-6} Torr). Height scale bar is ± 10 nm. Following the solid lines, we measure a height of ~ 3.9 nm after each process.

14. EDX spectrum of $PtSe_2$

For determining the elemental analysis of $PtSe_2$ crystal, we characterize its energy-dispersive x-ray (EDX) spectra. Supplementary Fig. 17 shows the EDX spectrum of $PtSe_2$ deposited on a carbon tape. The spectra show signals of carbon, oxygen, platinum and selenide. We believe that the detected carbon signal is due to the carbon substrate. It is absent if the crystal is

transferred onto an SiO_2 substrate. There is no element detected apart from oxygen, platinum and selenium which rules out the possibility of any intercalation process during growth. The presence of oxygen was also detected in a previous study.[11]

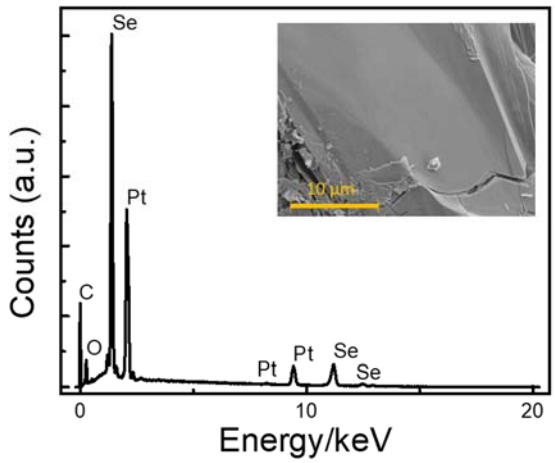

Supplementary Fig. 17. EDX spectrum of $PtSe_2$. EDX analysis of $PtSe_2$. Inset shows the SEM image of the crystal.

15. Calculation of ΔR

In this section, we discuss how the change in device resistance ΔR is calculated. Figure S18a shows the dependence of the device resistance on the magnetic field sweep directions. Resistance values for both backward and forward sweep directions are nearly identical above coercive fields of ~ 25 mT. By using a polynomial function, we perform the fitting for the magnetic field dependence of the device resistance by excluding the data between -25 mT < B < 25 mT range. After this, we subtract hte background fitting line from the measurement curves to calculate the change in device resistance due to the MR effect (Supplementary Fig. 18).

Similar background resistance subtraction has been also employed for spin valve curves to extract the spin-dependent contribution to the resistance.

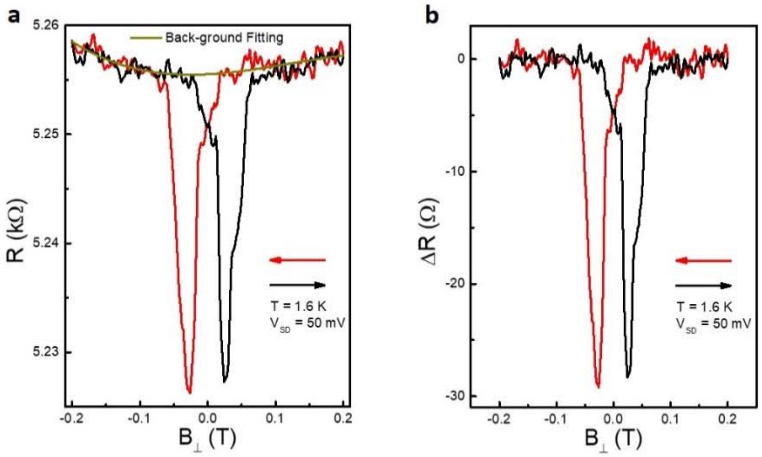

Supplementary Fig. 18. Subtracting the background signal. a, Magnetoresistance of $PtSe_2$ as a function of the out-of-plane magnetic field. Red and black arrows represent the sweep direction. Solid yellow line represents the polynomial fitting as described above. **b,** The change in the device resistance upon application of forward and backward sweep directions, after background subtraction.

REFERENCES

1. Ciarrocchi, A., Avsar, A., Ovchinnikov, D. & Kis, A. Thickness-modulated metal-to-semiconductor transformation in a transition metal dichalcogenide. *Nat. Commun.* **9**, 919 (2018).
2. Yu, X. *et al.* Atomically thin noble metal dichalcogenide: a broadband mid-infrared semiconductor. *Nat. Commun.* **9**, 1545 (2018).
3. Qi, L., Wang, Y., Shen, L. & Wu, Y. Chemisorption-induced n-doping of MoS_2 by oxygen. *Appl. Phys. Lett.* **108**, 063103 (2016).
4. Balakrishnan, J., Kok Wai Koon, G., Jaiswal, M., Castro Neto, A. H. & Özyilmaz, B. Colossal enhancement of spin–orbit coupling in weakly hydrogenated graphene. *Nat. Physics* **9**, 284–287 (2013).
5. Doganov, R. A. *et al.* Transport properties of pristine few-layer black phosphorus by van der Waals passivation in an inert atmosphere. *Nat. Commun.* **6**, 6647 (2015).
6. Zhao, Y. *et al.* High-Electron-Mobility and Air-Stable 2D Layered $PtSe_2$ FETs. *Adv. Mater.* **29**, 1604230 (2017).
7. Li, Z. *et al.* Anomalous magnetotransport behaviours in $PtSe_2$ microflakes. *J. Phys.: Condens. Matter* **29**, 23LT01 (2017).
8. Shcherbakov, D. *et al.* Raman Spectroscopy, Photocatalytic Degradation, and Stabilization of Atomically Thin Chromium Tri-iodide. *Nano Lett.* **18**, 4214–4219 (2018).
9. Island, J. O., Steele, G. A., Zant, H. S. J. van der & Castellanos-Gomez, A. Environmental instability of few-layer black phosphorus. *2D Mater.* **2**, 011002 (2015).
10. Avsar, A. *et al.* Air-Stable Transport in Graphene-Contacted, Fully Encapsulated Ultrathin Black Phosphorus-Based Field-Effect Transistors. *ACS Nano* **9**, 4138–4145 (2015).

11. O'Brien, M. *et al*. Raman characterization of platinum diselenide thin films. *2D Mater*. **3**, 021004 (2016).